

Evolution of brightness and magnetic features of young solar-type stars – I. The young G star HIP 89829

G. M. Perugini,¹★ S. C. Marsden,¹ I. A. Waite,¹ S. V. Jeffers,² N. Piskunov,³ N. Shaw,¹† D. M. Burton,¹ M. W. Mengel,¹ J. E. Hughes¹ and E. M. Hébrard⁴

¹Centre for Astrophysics, University of Southern Queensland, Toowoomba, QLD 4350, Australia

²Max Planck Institute for Solar System Research, Justus-von-Liebig-Weg 3, D-37077 Göttingen, Germany

³Department of Physics and Astronomy Uppsala University, SE-75120 Uppsala, Sweden

⁴Private Astronomer

Accepted 2021 September 16. Received 2021 September 14; in original form 2021 May 5

ABSTRACT

The evolution in latitude of sunspots is a key feature of the cyclic solar dynamo. Here, we present the results of a spectroscopic and spectropolarimetric monitoring campaign on the young (~ 20 Myr old) early G star HIP 89829, in order to investigate potential evolution in the distribution of the star's spots and magnetic features. Our analysis of this G5V star spans eight epochs, from June 2010 to August 2015. The techniques of Doppler imaging and Zeeman–Doppler imaging were used to create brightness maps for each epoch and magnetic maps for two epochs. The brightness images show the star to have stable spot features with two main spot latitudes – a polar spot, often seen on young rapidly rotating stars such as this, and another highly unusual group of large spot features around the 20° and 30° latitudes. These lower spot latitudes appear to be rather stable over the 5 yr of observations. We included a solar-type differential rotation law into the imaging process and measured near-solid-body rotation for epochs where sufficient data exist for this analysis. The magnetic features show a dominant poloidal and a weaker toroidal magnetic field for both Stokes V epochs, which is unusual for a star with a rapid rotation period of 0.57 d. We conclude that HIP 89829 is an active young solar-type star with long-lived spots and near-solid-body rotation.

Key words: line: profiles – stars: individual: HIP 89829 – stars: magnetic field – stars: solar-type – starspots.

1 INTRODUCTION

It has been known since 1843 that sunspot numbers are periodic in nature (Schwabe 1843), and in 1860, it was discovered that the Sun rotated faster at the equator than at the poles (Carrington 1860). In 1904, it was shown that sunspot distribution had a periodicity, the spots varying with the regular magnetic cycle in a pattern now famously known as the Maunder Butterfly Diagram (Maunder 1904). Four years later, George Ellery Hale published his discovery of magnetic fields in sunspots (Hale 1908).

We now know that magnetic fields are responsible for nearly all of the activity and variability of solar-type stars. This relationship between the magnetic field and sunspot activity shows that the Sun's magnetic dynamo is also cyclical, and we can see regular changes in this dynamo by the resulting sunspot activity. If we can infer that solar-type stars would have a similar magnetic dynamo, then we should be able to see star-spot migration in these stars as well.

Given that changes in sunspot numbers are associated with the strength of emission cores in the Ca II, H, and K lines, astronomers have used spectroscopy of other stars to analyse changes in these lines, searching for similar patterns in terms of star-spot periodicity, number density, and latitude distribution that would show magnetic

cycles similar to the Sun. The Mount Wilson H&K survey was initiated in 1966 by Olin Wilson (Wilson & Woolley 1970; Wilson 1976) to study stellar activity cycles in this manner, studying some 2000 stars throughout the project's lifetime. Of the dwarf stars studied, 60 per cent showed cyclical behaviour similar to the Sun, 25 per cent were variable but not cyclical, and 15 per cent showed flat activity (Baliunas et al. 1995).

It is still unknown exactly how a young star generates its magnetic field, or how they progress from irregular to regular cycles. When a star ages and its stellar rotation rate decreases, the underlying dynamo appears to be impacted; young active solar-type stars show more evidence of irregular or chaotic cycles than mature stars, and stars with slower rotation rates exhibit longer cycles (Baliunas et al. 1995). Understanding the nature of star-spot distributions for young active solar-type stars will lead to a better understanding of the underlying magnetic dynamo and how these cycles develop and mature over time.

The development of surface imaging techniques such as Doppler imaging (DI) (Vogt & Penrod 1983) and Zeeman–Doppler imaging (ZDI) (Semel 1989) has allowed for the analysis of the evolution of stellar magnetism both in strength and distribution, providing insight into the stellar dynamo (Donati et al. 2003; Marsden et al. 2011a; Waite et al. 2011). Additionally, these techniques can be used to study the level of surface differential rotation on a star, thought to be one of the key ingredients in both the solar and stellar dynamo (Petit, Donati & Collier Cameron 2002; Marsden et al. 2011b; Waite et al. 2015).

* E-mail: gregory.perugini@usq.edu.au

† Deceased.

Table 1. Fundamental parameters of HIP 89829 used/found in this study.

Parameter	Value
Right ascension ^a	18 ^h 19 ^m 52.21
Declination ^a	−29° 16′ 32.4
Distance ^a	79.22 ± 0.35 pc
Period ^a	0.57075 d
Luminosity ^a	1.64 ± 0.02 L _⊙
Classification ^b	G5V
Photospheric temperature ^a	5650 ± 50 K
Spot temperature ^c	3900 ± 50 K
Age ^d	~20 Myr
Mass ^d	~1.2 M _⊙
Radius ^e	1.95 ± 0.02 R _⊙
$v \sin i$ ^e	111.0 ± 1.0 km s ^{−1}
Inclination angle ^e	40° ± 5°
Radial Velocity ^e	−5.9 ± 0.3 km s ^{−1}

^aGAIA (2016); Brown et al. (2018).

^bTorres et al. (2006).

^cBerdyugina (2005).

^dBaraffe et al. (2015).

^eThis study.

A large enough time-span of observations must be available to identify cyclical latitudinal spot distribution, and only a few young stars have been studied for this to date. Continuous Period Search (CPS) analysis was conducted using photometry and time-series analysis (Lehtinen et al. 2016), and the results showed little evidence of cyclical spot distribution (although active longitudes were observed on the more active stars). The K2V star LQ Hya has what appears to be a 13-yr star-spot cycle, with additional data needed to confirm this (Lehtinen et al. 2012). The pre-main-sequence K0 dwarf star AB Doradus has been extensively studied using ZDI/DI (Cameron & Donati 2002; Donati et al. 2003; Jeffers, Donati & Collier Cameron 2007) with no evidence of cyclic behaviour in either the latitude distribution of spots or the spot coverage percentages. The G2V star V899 Her was also studied using ZDI/DI and was found to have stable spot latitude distributions over 19 epochs from 1999 to 2017 (Marsden et al. 2006; Jeffers & Donati 2008; Jeffers et al. 2011; Willamo et al. 2019). Additionally, the growing field of asteroseismology has produced some promising results and has been used to find active latitude variations for G8V star HD 173701 (Bazot et al. 2018). That study produced the first asteroseismic butterfly diagram spanning 17 quarters of Kepler data, with the results indicating some latitudinal fluctuation in active regions, but the periodicity was uncertain.

This paper is the first in a series to add to this growing field. Herein, we will be providing analysis of a fast rotating young G5V solar-type star HIP 89829, reconstructing its brightness topology over eight epochs spanning 5 yr. We present its basic parameters in Section 2, and in Section 3, we detail our methodology for extracting the observation data. In Section 4, we give the results of our DI and differential rotation. We follow this with a discussion of the results and analysis regarding HIP 89829’s latitude spot variation, differential rotation, and other fundamental parameters (Section 5).

2 HIP 89829 PARAMETERS

Table 1 gives an overview of the fundamental parameters of HIP 89829 (HD 168210). This star is reported as a single G5V star

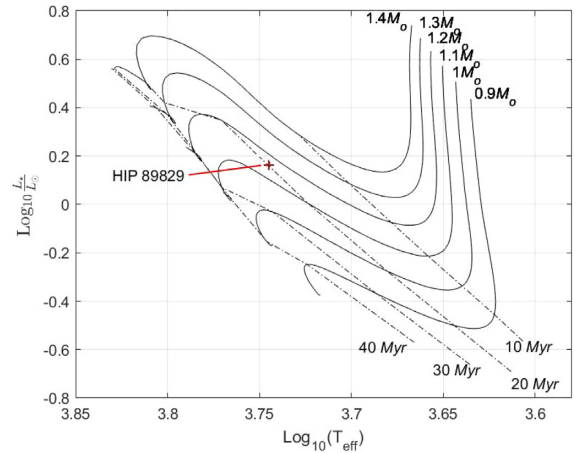


Figure 1. The evolutionary status of HIP 89829 using isochrones from the Baraffe evolutionary model (Baraffe et al. 2015). The solid lines are pre-main-sequence evolutionary tracks for stellar masses of 0.9–1.4 M_⊙ in 0.1 M_⊙ steps. The dot–dashed lines are age isochrones for stellar ages of 10, 20, 30, and 40 Myr.

(Torres et al. 2006; Waite et al. 2011) at a distance of 79.22 ± 0.35 pc, with a luminosity of 1.64 ± 0.02 L_⊙, as measured by the European Space Agency’s GAIA mission (GAIA 2016; Brown et al. 2018). The GAIA data also estimate an effective temperature of 5506 ± 50 K, which is in close agreement with the B–V flux derived temperature of 5615 K as found using the formulations of Bohm-Vitense and Ballesteros (Bohm-Vitense 1981; Ballesteros 2012). For G5V stars, the spot temperature can be estimated as ~1750 K less than photospheric temperature (Berdyugina 2005). Thus, we assume a spot temperature of ~3900 K.

When placing this star on theoretical pre-main-sequence isochrones (Baraffe et al. 2015), the age of this star is estimated to be ~20 Myr, with a mass of ~1.2 M_⊙, as shown in Fig. 1. The age estimate agrees with its high-probability membership in the Beta Pictoris group of approximately 20 stars with estimated ages of 20–26 Myr (Torres et al. 2008).

Several of our initial parameters were found using the DI code employed to reconstruct the images (see Sections 4.1 and 4.2). This was done using a χ^2 minimization technique, varying the selected parameter incrementally until χ^2 is minimized. See Jeffers & Donati (2008) and Marsden et al. (2005) for a full description of this methodology. This technique was used to discover or verify HIP 89829’s parameters of $v \sin i$, inclination angle, period, and radial velocity.

The $v \sin i$ found using this χ^2 minimization technique was 111.0 ± 1.0 km s^{−1}. This compares well with the published value of 114 ± 2.4 km s^{−1} (Torres et al. 2006). An inclination angle of 40° ± 2° was found using this technique, implying a radius of 1.95 ± 0.2 R_⊙. The radius reported by GAIA is 1.41 ± 0.02 R_⊙ (this discrepancy is discussed in Section 5.2).

With HIP 89829, we are fortunate to have four epochs taken over a time-base of 43 d, and this allows us to use this same χ^2 minimization technique to refine the equatorial rotation period of 0.571 d as given in the ROSAT study (Messina et al. 2010; Kiraga 2012) to 0.57075 ± 0.0001 d or $\Omega_{\text{eq}} = 11.008647$ rad d^{−1}.

The χ^2 minimization technique is optimized to a radial velocity of −5.9 ± 0.3 km s^{−1}. This is somewhat different from the previously reported measurement of −7.0 ± 2.6 km s^{−1} (Torres et al. 2006), but it is within the margin of error and is consistent across all epochs.

Table 2. Summary of the HIP 89829 observations.

Epoch/ Observatory	UT date	UT begin	UT end	Number of exposures
2010.494	2010 June 28	12:07:55	18:05:20	19
2.3-m	2010 June 29	10:11:51	18:14:07	26
2010.556	2010 July 21	10:37:12	16:05:57	21
2.3-m	2010 July 22	9:42:03	16:41:57	26
2010.597	2010 August 3	9:39:45	12:58:19	11
2.3-m	2010 August 4	8:45:27	15:13:49	26
	2010 August 5	8:42:09	14:25:09	22
	2010 August 6	8:40:16	12:55:52	17
	2010 August 7	11:01:41	12:48:49	8
	2010 August 8	9:16:08	9:31:24	2
2010.613	2010 August 7	0:58:37	3:44:25	8
3.6-m	2010 August 9	0:58:02	6:07:22	12
	2010 August 12	1:54:29	5:24:29	12
	2010 August 13	1:52:16	5:19:54	12
2011.378	2011 May 14	4:27:52	9:16:16	12
3.6-m	2011 May 15	4:26:17	9:15:17	8
	2011 May 16	4:00:43	9:35:25	12
	2011 May 17	2:45:35	9:54:04	12
	2011 May 18	3:36:24	9:49:55	12
	2011 May 19	3:17:58	8:58:38	8
	2011 May 20	3:03:25	3:57:45	4
2011.484	2011 June 24	10:22:48	18:21:45	31
2.3-m	2011 June 26	10:44:59	18:47:05	27
2012.272	2012 April 7	14:40:51	19:25:15	15
2.3-m	2012 April 8	17:01:58	19:11:34	7
	2012 April 9	14:51:22	16:38:04	8
2015.511	2015 July 2	14:30:12	18:49:32	9
2.3-m	2015 July 3	9:28:13	18:17:34	12
	2015 July 5	9:19:44	18:14:15	18
	2015 July 6	8:51:56	18:25:55	18
	2015 July 7	8:49:55	18:15:24	18

Note. Epochs 2010.613 and 2011.378 are spectropolarimetric observations from the HARPSpol instrument on the ESO 3.6-m telescope at La Silla observatory in Chile. All others are from the Échelle instrument on the ANU 2.3-m telescope at Siding Spring Observatory in New South Wales, Australia.

3 HIP 89829 OBSERVATIONS

3.1 Observation overview

Both spectroscopic and spectropolarimetric data were obtained for HIP 89829 over eight epochs from June 2010 to July 2015. A summary of these observations is given in Table 2.

Six of these epochs (2010.494, 2010.556, 2010.597, 2011.484, 2012.272, and 2015.511) are spectroscopic data and were obtained using the Australian National University's (ANU) 2.3-m telescope and a high-resolution Échelle spectrograph, located at the Siding Spring Observatory (SSO) in New South Wales, Australia (Burton 2013). This spectrograph has a 79 grooves mm^{-1} grating, providing a wavelength coverage of 426–684 nm, with a resolution of $R \sim 24,000$. The spectrograph camera is a $2\text{k} \times 2\text{k}$ pixel E2V CCD detector with $13.5\text{-}\mu\text{m}$ square pixels.

Spectropolarimetric data for 2010.613 and 2011.378 were obtained using the European Southern Observatory (ESO) 3.6-m telescope, located in La Silla, Chile. The spectra were obtained by the High Accuracy Radial Velocity Planet Searcher spectrograph equipped with the polarimetric unit (HARPSpol), installed at the Cassegrain adapter directly below the primary mirror (PHASE 2003; Rupprecht

Table 3. Summary of DI data extraction results for HIP 89829.

Epoch Date	Number of observations	Mean LSD signal-to-noise ratio	Spot coverage percentage ^a
2010.494	45	834	4.62
2010.556	47	930	4.44
2010.597	86	833	5.10
2010.613	44	1239	5.88
2011.378	68	1303	4.69
2011.484	59	952	3.67
2012.272	30	922	6.07
2015.511	75	1043	4.85

^aAs a per cent of stellar surface.

et al. 2004). HARPSpol has a 257.17 grooves mm^{-1} grating with a spectral range of 378–691 nm and a resolution of $R \sim 115,000$. The CCD detector is $4\text{k} \times 4\text{k}$, with $15\text{-}\mu\text{m}$ pixels. Observations were taken in polarimetric mode (Stokes V) and both left- and right-hand circularly polarized light was obtained simultaneously.

3.2 Observation methodology and reduction

Table 3 summarizes the data extraction results for each epoch. The observation epochs each span enough time to provide full-phase coverage of HIP 89829 given the 0.57075 d rotation period. The rotation phase for each observation was obtained by the use of the following ephemeris:

$$\text{HJD} = 2455374.0 + 0.57075\phi, \quad (1)$$

where HJD is the heliocentric Julian date of the observation and ϕ is the rotational phase. The date of 2355374.0 was chosen arbitrarily as 2 d before the first observation of the first epoch, and used for each epoch to standardize phasing.

The mean pixel resolution for the 2.3-m spectra was determined to be 4.1 km s^{-1} per pixel, and for the HARPSpol spectra, it was determined to be 1.6 km s^{-1} per pixel. The ESPRIT (Échelle Spectra Reduction: an Interactive Tool) software package (Donati & Cameron 1997; Donati et al. 2003) was used with standard calibration frames to extract normalized spectra for the 2.3-m observations, and LIBRE-ESPRIT was used in the same fashion for the HARPSpol observations. Least-squares deconvolution (LSD) is then applied, which utilizes the large number of photospheric lines available in the Échelle spectrum to produce a least-squares profile through cross-correlation, vastly increasing averaged signal-to-noise ratio (S/N). This method has been used successfully to determine the surface structure on a number of solar-type stars (Barnes et al. 2000; Donati et al. 2000; Barnes & Collier Cameron 2001; Jeffers, Barnes & Collier Cameron 2002; Barnes et al. 2004). For the 2.3-m observations, the S/N increased from ~ 100 to ~ 900 using LSD. The HARPSpol observations had an S/N increase from ~ 200 to ~ 1250 . For the 2.3-m observations, we also utilized ESPRIT to shift the wavelength-calibrated spectrum from the 2.3-m telescope to match the LSD profile of the telluric lines contained in the spectra, thus correcting for minor instrumental shifts in wavelength space due to atmospheric temperature and pressure variations. This reduced the errors in radial velocity shifts of the LSD profiles to the order of 0.1 km s^{-1} . This correction was not necessary for the HARPSpol observations due to its inherent stability.

Stokes I LSD profiles were extracted successfully from all eight epochs using the methodology above. In addition, Stokes V LSD profiles were obtained from the HARPSpol observations (epochs 2010.613 and 2011.378).

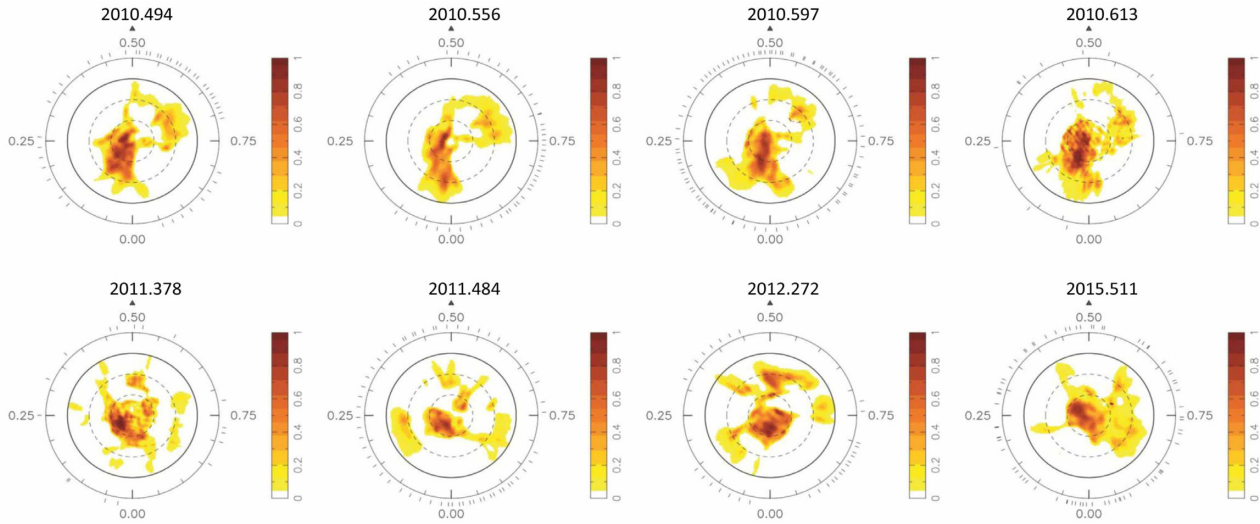


Figure 2. Stokes I spot occupancy plots for HIP 89829 over all eight epochs, using maximum entropy brightness image reconstruction. The images are flattened polar projections from the north pole viewpoint down to -30° latitude. The $+30^\circ$ and the $+60^\circ$ latitudes are shown as dotted lines, and the equator is shown in bold. The radial ticks outside the plots indicate the observation phases, with spot occupancy varying from 3.67 per cent for epoch 2010.484 to 6.07 per cent for epoch 2012.272 as given in Table 3.

4 RESULTS

4.1 Parameters for image reconstruction

Given these LSD profiles, we reconstructed the surface brightness images and the magnetic topologies of HIP 89829. Using these images and the outputs, we can also analyse the differential rotation and spot latitude distributions (see Sections 4.4 and 5.1).

In addition to the reduced LSD profiles, this code requires several key inputs, including photospheric and spot temperatures, heliocentric radial velocity, $v \sin i$, and inclination angle. Table 1 lists the fundamental parameters used in the image reconstruction.

4.2 Stokes I image reconstruction

The DI of HIP 89829 was achieved by using a maximum entropy code (Brown et al. 1991; Donati et al. 1997). Using this code and the fundamental parameters, we performed brightness imaging on the stellar surface of HIP 89829 for each epoch. The code uses the maximum entropy optimization algorithm to produce maps with the minimum required information (i.e. spots) needed to fit the data to the required level (Skilling & Bryan 1984). The maximum entropy code uses a two-component brightness model (Cameron 1992), with a value of 1 corresponding to full spottedness and 0 being a unspotted photosphere. In Table 3, we give the spot percentage occupancy as a function of the entire stellar surface for each epoch, and show the results of the image processing in Fig. 2. The images are created assuming solid-body rotation (see Section 4.4).

Figs A1–A8 display the maximum entropy Stokes I intensity fits to the LSD profiles for each of the eight epochs. The modelled fits (black lines) are compared to the observed LSD profiles (red lines).

4.3 Stokes V magnetic field topology

We obtained magnetic field maps for the 2010.613 and 2011.378 epochs (Figs 3 and 4) using the mapping code of Donati & Brown (1997), which includes spherical harmonic expansions of the magnetic field (Donati et al. 2006). As has been done in previous

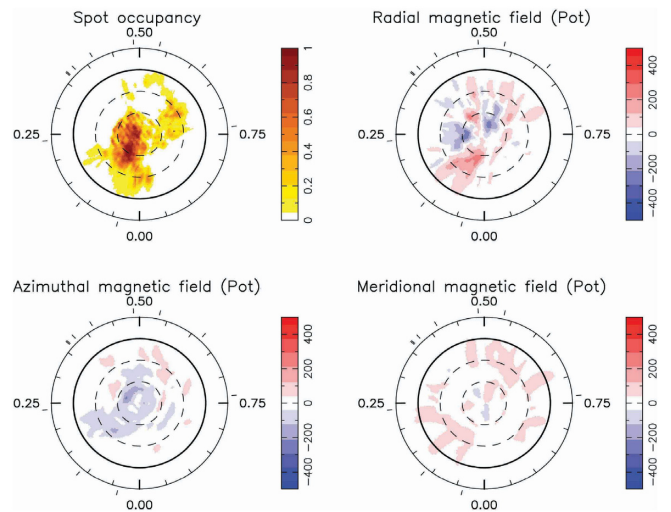


Figure 3. Stokes V maximum entropy brightness and magnetic image reconstructions for HIP 89829, epoch 2010.613. The spot mapping is reproduced from Fig. 2, with the scale of the magnetic images in Gauss. The spot map in the upper left-hand panel shows a 5.88 per cent spot occupancy, while the global magnetic field strength is 43.8 G.

research, we used a weighting scale that favours lower ℓ values for comparison to other magnetic topology research (Petit et al. 2008; Marsden et al. 2011a; Waite et al. 2011). The maximum harmonic expansion of $\ell_{\max} = 50$ was selected in that any successive increases gave no discernible changes to the magnetic topologies.

The reduced χ^2 value was set to 1.0 for both epochs to produce the magnetic maps, showing the fit accuracy very close to the noise level for the data. This resulted in a mean field strength of 43.8 G for epoch 2010.613 and 75.4 G for epoch 2011.378. Figs 3 and 4 show these maps for each respective epoch, with the brightness image (top left-hand panel) reproduced for comparison. Figs A9 and A10 show the fits to the Stokes V LSD profiles for these two epochs. A poloidal plus

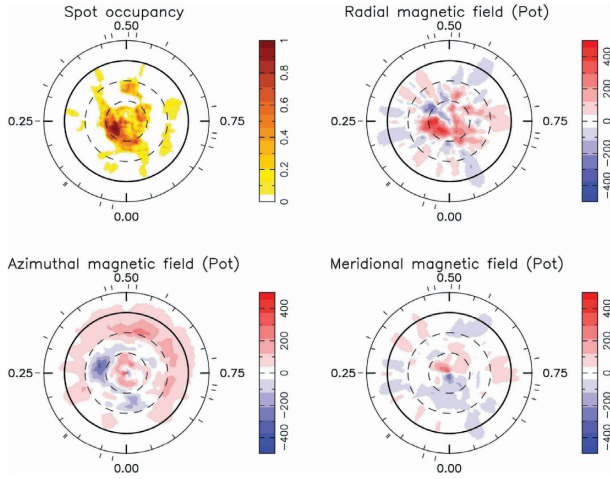


Figure 4. Stokes V maximum entropy brightness and magnetic image reconstructions for HIP 89829, epoch 2011.378. Scale in mapping is the same as in Fig. 3, with spot map reproduced from Fig. 2. The spot map shows a 4.69 per cent spot occupancy, and the magnetic field maps have a global strength of 75.4 G.

Table 4. Magnetic quantities derived from magnetic maps in Figs 3 and 4.

Quantity	Epoch 2010.613 (per cent)	Epoch 2011.378 (per cent)
Percent poloidal energy	77 ⁺² ₋₃	62 ⁺² ₋₆
Percent toroidal energy	23 ⁺¹ ₋₂	38 ⁺⁶ ₋₃
Percent poloidal ($l = 1$)	15 ⁺¹ ₋₁	21 ⁺² ₋₃
Percent poloidal ($l = 2$)	11 ⁺¹ ₋₁	6 ⁺⁰ ₋₀
Percent poloidal ($l = 3$)	8 ⁺¹ ₋₁	6 ⁺¹ ₋₁
Percent poloidal ($l \geq 4$)	66 ⁺¹ ₋₁	65 ⁺³ ₋₉
Percent toroidal ($l = 1$)	0 ⁺¹ ₋₀	20 ⁺¹ ₋₂
Percent toroidal ($l = 2$)	12 ⁺¹ ₋₂	9 ⁺¹ ₋₀
Percent toroidal ($l = 3$)	18 ⁺² ₋₁	18 ⁺¹ ₋₃
Percent toroidal ($l \geq 4$)	71 ⁺¹ ₋₄	55 ⁺² ₋₂
Percent axisymmetry poloidal	39 ⁺² ₋₃	49 ⁺¹ ₋₃
Percent axisymmetry toroidal	67 ⁺⁵ ₋₁	77 ⁺⁴ ₋₃

Given are the percentages of the large-scale magnetic energy of the reconstructed poloidal and toroidal components. These energies are each then segregated into poloidal and toroidal l values of 1, 2, and 3, respectively. Higher order energies ($l \geq 4$) are summarized for poloidal and toroidal, respectively. The last two rows show the percentages of the poloidal and toroidal fields that are axisymmetric ($m = 0$). Per cent variations were obtained by increasing and decreasing $v \sin i$ by 2.0 km s^{-1} , inclination angle by 5° , and differential rotation by one standard deviation.

toroidal field was assumed for both epochs. The magnetic quantities derived from the maps are given in Table 4.

4.4 Differential rotation

DI can be used to map the movement of the spots over time, allowing for a direct method of measuring the stellar surface rotation at different latitudes. We can calculate the amount of shear over time using a solar-type differential rotation law:

$$\Omega(\theta) = \Omega_{\text{eq}} - d\Omega \sin^2 \theta, \quad (2)$$

Table 5. Summary of differential rotation results for HIP 89829.

Epoch	Ω_{eq} rad d ⁻¹	$d\Omega$ rad d ⁻¹
2010.494	11.084 ± 0.023	0.146 ± 0.052
2010.523^a	11.279 ± 0.001	0.001 ± 0.002
2010.556	11.103 ± 0.022	0.228 ± 0.050
2010.597	11.028 ± 0.006	0.041 ± 0.012
2010.613	10.977 ± 0.005	−0.078 ± 0.008
2011.378-I	11.041 ± 0.053	−0.009 ± 0.009
2011.378-V	11.071 ± 0.008	−0.009 ± 0.016
2011.484	10.880 ± 0.021	0.002 ± 0.036
2012.272	11.233 ± 0.029	−0.025 ± 0.041
2015.511	11.045 ± 0.005	0.054 ± 0.009

Note. These values were arrived at by treating Ω_{eq} and $d\Omega$ as free parameters and varying these in successive pairs to find an optimized χ^2 . The errors are one standard deviations. Plots for each epoch are shown in Fig. 5. Entry 2010.523 displays the results of combining 2010.494 and 2010.556 as one epoch. Epoch 2011.378 is shown with two entries, for Stokes I and Stokes V . Those epochs in bold meet the sufficient requirements for accurate measurement of differential rotation, as explained in Section 4.4. ^aCombination of epochs 2010.494 and 2010.556.

where $\Omega(\theta)$ is the rotation rate at latitude θ , Ω_{eq} is the equatorial rotation rate, and $d\Omega$ is the rotational shear between the equator and the poles (the differential rotation). To measure differential rotation, we can treat Ω_{eq} and $d\Omega$ as free parameters and determine the best fitting to the data using χ^2 minimization. The results are shown for each epoch in Table 5 and Fig. 5. We discount the differential rotation results for epochs 2010.494, 2010.556, 2011.484, and 2012.272 for several reasons. The accuracy of differential rotation measurements depends strongly on the number of observations per day, the number of days of observations, and the resolution of the spectra obtained. There also needs to be sufficient phase coverage and time for the star to evolve under the influence of differential rotation, as well as high enough resolution to reveal possible shifts.

Epochs 2010.494, 2010.556, and 2011.484 only have 2 d of observations, and 2012.272 only has 3 d of observations. We should also note that the observation sessions of epoch 2011.484 are separated by a day. The time-bases for these four epochs, while enough for DI, are potentially not long enough to allow the spots to evolve under the influence of differential rotation, so the differential rotation results from these epochs are treated as unreliable.

The two epochs from the HARPSpol along with the 2010.494 and 2015.556 epochs from the 2.3-m telescope give us adequate specifications for consistent differential rotation results. The HARPSpol epochs (2010.613 and 2011.378) have higher resolution and sufficient observations spread over 6 d (44 and 56 observations, respectively). Although the 2010.597 and 2015.511 observations are acquired using the lower resolution 2.3-m telescope with the Échelle spectrograph, they each have a large time-span (6 and 5 d, respectively) and a large enough number of observations (86 and 75, respectively) to give reasonable differential rotation measurements (although the error bars may be underestimated, as we discuss in Section 5.4).

Epochs 2010.494 and 2010.556 by themselves do not have sufficient time-span or number of observations to meaningfully resolve differential rotation, but given they have very similar Doppler maps, we combined these epochs into one epoch (2010.523) and performed DI and differential rotation analysis. The χ^2 minimization optimized at a reasonable value of 0.45 when compared to the originating epoch

values of 0.35 for 2010.494 and 0.40 for 2010.556 – only slightly higher even with the 22-d time gap between the epochs. The resulting Doppler map was very similar to the individual image maps, and the differential rotation values for this analysis are also included in Table 5.

In Fig. 5, we show differential rotation reduced χ^2 landscapes for each epoch using the Stokes I data. Using the stellar parameters given in Table 1 and the spot coverage from Table 2, the landscapes were created by systematically varying the differential rotation parameters Ω_{eq} and $d\Omega$, with the darker colours representing lower χ^2 values. The error bars shown are calculated by varying $v \sin i$ ($\pm 2 \text{ km s}^{-1}$), inclination angle ($\pm 5^\circ$), and spot coverage (± 5 per cent). A 1σ paraboloid encompasses these error bars. In Fig. 6, we show the differential rotation plot using the Stokes V data for the 2011.378 epoch. It was created in the same way as the Stokes I data, with the paraboloid and error bars being added in the same manner. We varied the magnetic field (± 10 per cent) instead of varying spot coverage. We were not able to produce a meaningful χ^2 landscape for epoch 2010.613.

5 DISCUSSION AND ANALYSIS

5.1 Spottedness and latitude distribution

The latitudinal distribution of the spots can be plotted in terms of fractional spottedness, defined as

$$F(\theta) = \frac{S(\theta)\cos(\theta)d\theta}{2}, \quad (3)$$

where $S(\theta)$ is the average spot occupancy at a given latitude θ and $d\theta$ is the width of each latitude ring. This is plotted for all epochs in Fig. 7. On this graph and in Fig. 2, we see the polar spots that are typical with other fast rotators such as R58 (Marsden et al. 2005), AB Dor (Donati et al. 2003), V530 Per (Cang et al. 2020), and LQ Lup (Donati et al. 2000). But in addition to this, we find large stable star-spot structures around the 20° and 30° latitudes. This is highly unusual for such a rapidly rotating star and could possibly be caused by the lack of differential rotation discussed in Section 5.4.

It is important to note that the Doppler maps in Fig. 2 are all phase aligned from a common starting point as mentioned in Section 3.2 and equation (1). Although we can expect some drift in phase due to the accuracy of rotational parameters and the large span of 1830 d from the starting epoch of 2010.494 to the final one of 2015.511, we can clearly see that the spot structures are long-lived and rather stable. In the 43 d and 76 rotations covering the first four epochs, we see the spot features in similar patterns and in similar locations. In terms of spot coverage, we find some variability across epochs from 3.67 per cent to 6.07 per cent (see Table 3), but the latitude distribution is relatively consistent, showing little migration between epochs (Fig. 7).

In terms of solar-type cycles, none seems evident – if there was a pattern similar to the solar butterfly diagram, we would expect a migration in the latitude of the star-spot distribution between epochs 2010.494 and 2015.511, but as noted, we are not seeing any migration of star-spots. It cannot be ruled out that HIP 89829 may in fact have a cyclical pattern over a significantly longer time frame than we have here, but our results show no significant large-scale changes in the latitudinal distribution of star-spots over a 5-yr period. There is some indication of a lessening of the lower latitude spots in epochs 2010.613 and 2011.378 accompanied by an increase in spots at the 60° latitude, but the lower latitude spots return to the previous latitudes soon after.

5.2 Radius discrepancies with GAIA

The *GAIA DR2* estimate for the radius of HIP 89829 is approximately $1.4 R_\odot$ (Brown et al. 2018). We can determine the radius of HIP 89829 by using the equation

$$\text{Radius} = \left(\frac{v \sin i * \text{Period}}{2 * \pi * \sin(i)} \right). \quad (4)$$

We used χ^2 minimization analysis to find the inclination angle (i) for each epoch, finding that each epoch agrees with a consistent 40° inclination (see Fig. 8). Given this inclination angle and the values for $v \sin i$ and period as given in Table 1, the above equation

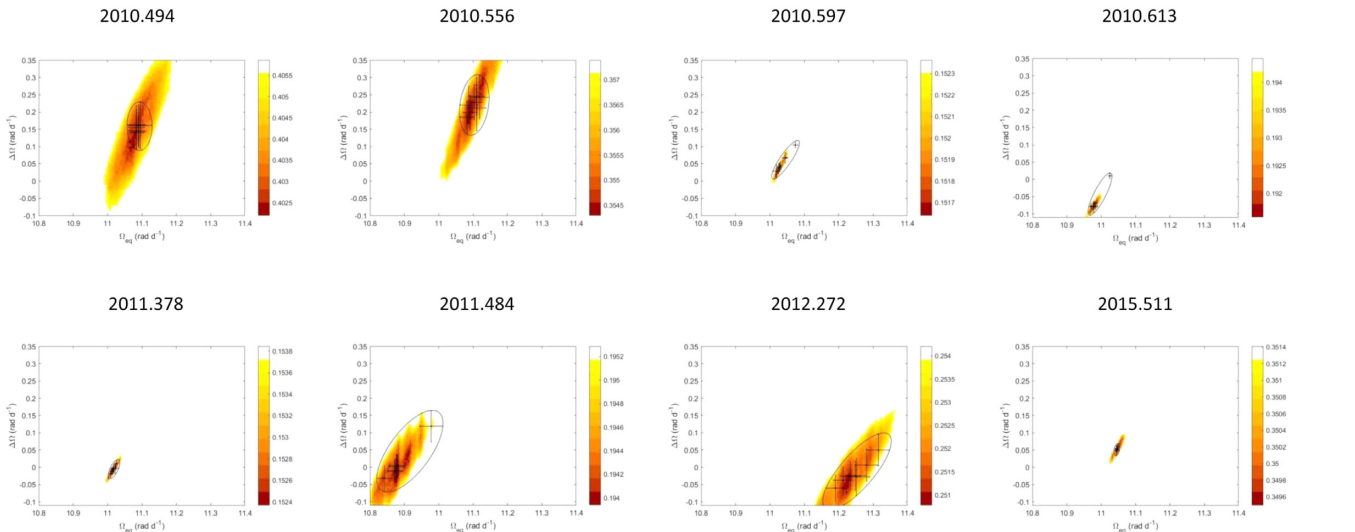


Figure 5. HIP 89829 differential rotation Stokes I plots, epochs 2010.494–2015.511. These χ^2 surface minimization landscapes are obtained by systematically changing the Ω_{eq} and $d\Omega$ pairs to arrive at an optimal parameter set with the lowest χ^2 value. This is a $\pm 5\sigma$ projection with darker colours indicating lower χ^2 values. The variation bars superimposed on each graph are 1σ variances generated by changing the star’s inclination ($\pm 5^\circ$), $v \sin i$ ($\pm 2 \text{ km s}^{-1}$), and the spot coverage (± 5 per cent)

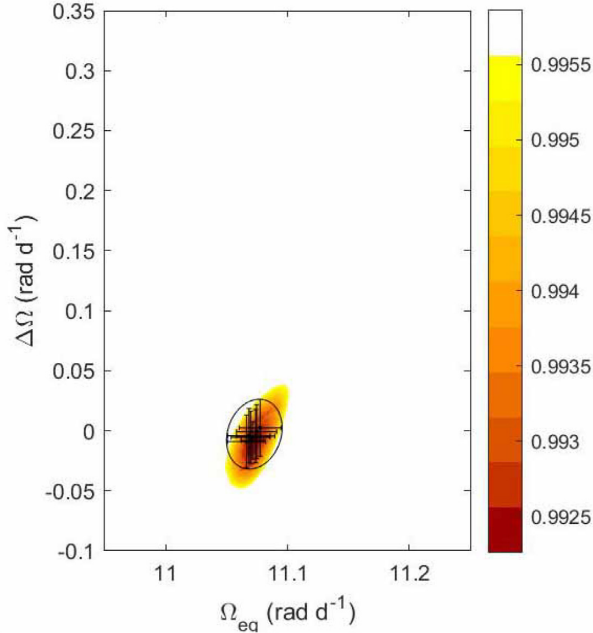


Figure 6. HIP 89829 differential rotation Stokes V plot for epoch 2011.378. This is a χ^2 surface minimization landscape, with a $\pm 3\sigma$ projection. Paraboloid and variation bars obtained in a similar manner to the Stokes I landscapes found in Fig. 5.

solves to a radius of approximately $1.95 R_{\odot}$. This is a large variance from the *GAIA DR2* estimate.

The initial parameters of $vsini$ and period have been verified by several sources. We can perhaps question the inclination angle estimate of 40° obtained displayed in Fig. 8, which shows the χ^2 minimization values obtained when varying the stellar inclination for the DI maps. Solving for inclination angle in equation (4) using the *GAIA* radius of $1.4 R_{\odot}$ yields a inclination angle of 63.3° . DI using this inclination shows a major increase in the amount of polar spots, but the locations of the spots are still consistent. Given that the results in Fig. 8 are extremely consistent over all epochs, we are inclined to believe our inclination angle findings of 40° . It is important to note that the *GAIA* radius estimate is derived assuming the Stephan–Boltzmann law and no extinction. In addition to this, the significant amount of spots on HIP 89829 and the number of long-lived low-latitude spots could be causing the *GAIA* inclination angle to be overestimated.

5.3 Stokes V magnetic map analysis

The magnetic maps for HIP 89829 have several features of note. The toroidal $l = 1$ field magnetic energy increases from $0.0^{+1 \text{ per cent}}_{-0 \text{ per cent}}$ in epoch 2010.613 to $20^{+1 \text{ per cent}}_{-2 \text{ per cent}}$ in epoch 2011.378, with a strong azimuthal magnetic field at the lower latitudes, as shown in Figs 3 and 4. This change between the two epochs (about 280 d apart) may also coincide with a migration of the azimuthal magnetic field from the polar to the equatorial regions. The 2010.613 epoch azimuthal map primarily shows large negative polarity in the polar region, while in the later epoch of 2011.378, we see a positive ring formation near the polar region, a negative ring in the 30° – 60° latitude, and then a strongly positive ring nearer the equator. This may be evidence of a ring migration, but we have only data for two epochs – further observations would be necessary to confirm this.

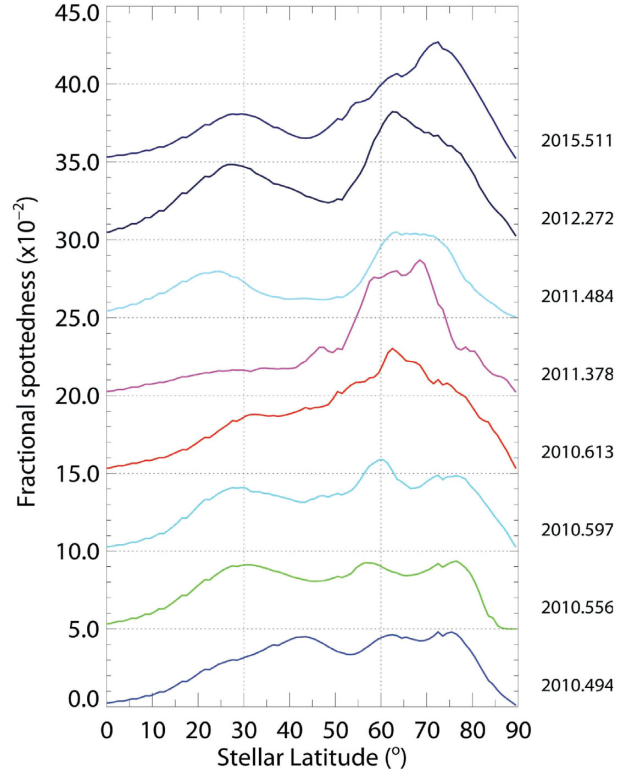


Figure 7. Fractional spottedness by latitude for all eight epochs of HIP 89829. Fractional spottedness is based on the average spot occupancy at each latitude and is defined by equation (3). Each epoch is shifted up by 5.0×10^{-2} for graphing purposes.

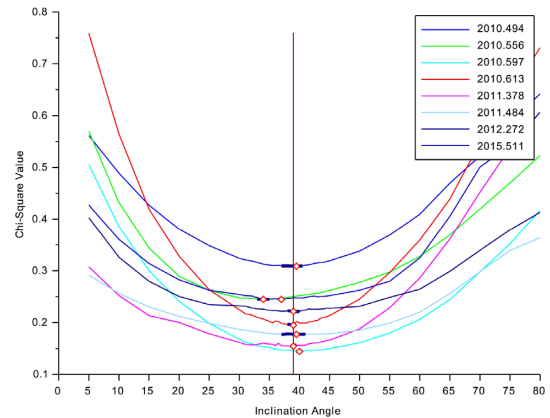


Figure 8. HIP 89829 inclination angle analysis for the DI maps in Fig. 2 using χ^2 minimization. Each epoch is plotted varying only the inclination angle in 1-deg increments. The red diamonds indicate the lowest χ^2 value for each epoch. The vertical line denotes a 40° inclination, and the blue wings indicate three standard deviations from the lowest values.

The poloidal-to-toroidal magnetic field ratio we find unusual as well. Previous research infers that fast solar-type stars with rotation periods of 12 d or less would have toroidal energy greater than poloidal energy, with the dominance becoming larger with higher rotation rates (Petit et al. 2008). Given HIP-89829’s fast rotation period of 0.57075 d, we thus would expect very dominant toroidal energy as a per cent of total energy. This is not the case, as given in Table 4; epochs 2010.613 and 2011.378 show poloidal energy

of 77^{+2}_{-3} per cent and 62^{+2}_{-6} per cent, respectively. Poloidal energy in HIP 89829 clearly dominates toroidal energy.

5.4 HIP 89829 solid body rotation

As was noted in Section 5.1, we have long-lived and stable spots across the epochs, which implies that HIP 89829 is rotating very much as a solid body. This is confirmed by the differential rotation results given in Table 5. We note that epochs 2010.597 and 2015.511 show closer to solar-type differential rotation (with the equator rotating faster than at the poles), but the error bars shown are likely underestimated due to the lower spectral resolution of these epochs. This is a reasonable conclusion when we see the large variance in differential rotation between epochs 2010.597 and 2010.613 even though they overlap.

When we combined the two early epochs of 2010.494 and 2010.556 into one epoch 2010.523 (see Section 4.4), we find a $d\Omega$ of 0.001 ± 0.002 rad d⁻¹. This closely matches the findings of the HARPSpol epoch 2010.613 of -0.078 ± 0.008 rad d⁻¹ and the HARPSpol epoch 2011.378 of 0.001 ± 0.002 rad d⁻¹, adding confirmation of our findings of near-solid-body rotation for HIP 89829.

In 2016, Balona & Abedigamba (2016) studied 2562 Kepler K, G, F, and A star photometry data, finding a complex relationship between differential rotation, effective temperature and rotation. They found a reasonable fit to the data with the following interpolation formula:

$$\text{Log}(d\Omega) = -211.12 + 109.67x - 11.14y - 14.30x^2 + 3.02xy, \quad (5)$$

where $x = \log(T_{\text{eff}})$ and $y = \log(\Omega_{\text{eq}})$, with Ω_{eq} and $d\Omega$ in rad d⁻¹.

HIP 89829, however, seems to be an exception to this predictive formula. Using the rotation rate and T_{eff} as noted in Table 1, the equation predicts a $d\Omega$ of 0.17 rad d⁻¹, which is over three times that of the Sun. This is in sharp contrast to the near zero value of differential rotation found in this paper.

Using HIP89829's parameters, the Baraffe pre-main-sequence stellar models (Baraffe et al. 2015) indicate a convection layer depth of 28.7 per cent of the stellar radius. A comparison of convection layer depth to differential rotation for young solar-type stars (Marsden et al. 2011b) indicates that HIP 89829 should have a differential rotation of 0.1 to 0.2 rad d⁻¹, which also agrees with equation (5). Again, we find near-solid-body rotation for HIP 89829 in our analysis.

5.5 Differential rotation of HIP 89829 in perspective

Given the unusual nature of the apparent solid-body rotation for HIP 89829, it is interesting to compare HIP 89829 to similar stars, which have had multiple-epoch imaging analysis. We note here that the $d\Omega$ of the Sun has been well established as 0.055 rad d⁻¹ (Balthasar, Vázquez & Wöhl 1986), and this agrees well with equation (5) results for a T_{eff} of 5780 K and period of 25.38 d.

As mentioned in the introduction, the young K0 dwarf star AB Dor has been extensively studied. Using 1995 data, AB Dor was initially found to have a $d\Omega$ value of 0.056 ± 0.012 rad d⁻¹ (Donati & Cameron 1997). This was confirmed by a subsequent study of three epochs from 1992 to 1994, finding 0.061 ± 0.006 , 0.071 ± 0.009 , and 0.074 ± 0.009 rad d⁻¹, respectively (Jeffers et al. 2007). A study of over five epochs from 1995 to 2001 revealed a close agreement when using Stokes *I* data, but they found a larger $d\Omega$ using Stokes *V*

data for the same epochs, ranging from 0.0596 ± 0.003 rad d⁻¹ in 1996 to 0.0967 ± 0.008 rad d⁻¹ in 1995 (Donati et al. 2003).

G2V Star V899 Her is a young fast-rotating star with a T_{eff} of 5808 K and a rotational period of only 1.33 d. In research thus far, we find a consistently high range of values for differential rotation – a 2004 epoch yielding a $d\Omega$ of 0.40 ± 0.04 rad d⁻¹ (Marsden et al. 2006), a 2005 epoch yielding a $d\Omega = 0.52 \pm 0.04$ rad d⁻¹ (Jeffers & Donati 2008), and a 2007 epoch yielding a $d\Omega$ of 0.4 ± 0.15 rad d⁻¹ (Jeffers et al. 2011).

ϵ Eridani is a young K2V star with a T_{eff} of 5146 ± 31 K. Three studies to date yield calculations of $d\Omega$ as 0.151 (Jeffers et al. 2014), 0.2 (Jeffers et al. 2017), and 0.11 rad d⁻¹ (Petit et al. 2021). This star is a good example of the strong correlation of rotation rate with differential rotation – although ϵ Eridani is smaller and cooler than our Sun, it has twice the differential rotation, most likely due to its rotation rate of 10.58 d (~ 2.5 times that of the Sun).

LQ Lup is a G8IV T-Tauri star, and also like HIP 89829 it is young (~ 25 Myr) and very rapidly rotating (period of 0.31 d), with a similar temperature (T_{eff} of ~ 5750 K). Given these parameters, we would expect a high differential rotation, and it was found to have a $d\Omega$ of 0.130 ± 0.02 rad d⁻¹ – between two and three times that of the Sun (Donati et al. 2000).

Although cooler than HIP 89829 with a T_{eff} of ~ 5280 K, the G8V star V530 Per has some similarities to HIP 89829 – it is of similar age (~ 30 Myr) and is rapidly rotating with a period of just 0.32 d. V530 Per was found to have a $d\Omega$ of 0.042 ± 0.005 rad d⁻¹, similar to the Sun. (Cang et al. 2020).

G2V star HD 141943 is of similar age to HIP 89829 (~ 17 Myr) and of similar temperature (T_{eff} of 5850 ± 100 K). Being a fast rotator with a period of ~ 2.2 d, we should expect it to have a high differential rotation, and for three epochs, we have $d\Omega$ values of 0.240 ± 0.030 , 0.360 ± 0.090 , and 0.450 ± 0.080 rad d⁻¹ (Marsden et al. 2011b).

HD 75332 is an older (~ 0.9 Gyr) F7V star with a T_{eff} of 6258 ± 44 K (Valenti & Fischer 2005), and it is plausible that HIP 89829 may evolve into a similar though slightly cooler solar-type star. Over 12 epochs between 2007 and 2019, HD 75332 was found to have a rotational period of approximately 3.56 d, with a $d\Omega$ of 0.25 ± 0.22 rad d⁻¹ (Brown et al. 2021).

F8V star τ Bootis is also older than HIP 89829 at ~ 0.9 Gyr, being slightly larger and slower with a period of 3.1 d. Like HD 75332, it also may be an analogue for what HIP 89829 may become as it ages. τ Bootis was analysed using ZDI/DI for 12 epochs with $d\Omega$ ranging from 0.10 ± 0.04 to 0.52 ± 0.15 rad d⁻¹ (Donati et al. 2008; Fares et al. 2009; Mengel et al. 2016; Jeffers et al. 2017). The Fourier transform method was also used to estimate differential rotation, finding $d\Omega$ to be 0.35 ± 0.14 rad d⁻¹ (Mengel et al. 2016).

While by no means comprehensive, the above stars have what we would expect for differential rotation, with each one being in broad agreement with the prediction of equation (5). Indeed, those stars with DI results to the date of the Balona study (Balona & Abedigamba 2016) were found to have a close correlation of $d\Omega$ with equation (5).

Given these examples, we should expect a young fast-rotating G5V star such as HIP 89829 to have a large shear, consistent with equation (5) and the convection depth analysis in Section 5.4. In contrast, we find near-solid-body rotation, and it is unknown what could cause this. In binaries, we may perhaps see tidal locking due to influences of the second star [see Hussain et al. (2006) on V471 Tau], but such a body would create a variance in radial velocity, and we see very little such variance in the eight HIP 89829 epochs studied (radial velocity of -5.9 ± 0.3 km s⁻¹).

6 CONCLUSION AND SUMMARY

This research spans 5 yr of observations on the young rapidly rotating star HIP 89829 with sufficient resolution to perform DI. We find long-lived spots and stable spot latitude distributions over the entire 5-yr time frame. We also find these large spot structures in the lower latitudes of 20° and 30°, which is highly unusual for a star with such a short rotational period.

We did not see any indication of a cyclical star-spot pattern. Further observations would be necessary to establish if a larger cyclical pattern exists.

The magnetic mapping shows a possible migration of the azimuthal magnetic field from pole to equator in the 280 d between the 2010.613 and 2011.378 epochs. The amount of toroidal field energy and rotation rate indicate a potentially very active dynamo, which is counter to the findings of long-lived spot patterns. We also find the magnetic field energy largely poloidal for both epochs, which is unusual for a fast rotating solar-type star.

The static spot distribution is consistent with our differential rotation analysis, showing near-solid-body rotation. Given that these observations are over eight epochs and two different observatories, we consider this solid-body rotation real and not an artefact of the data or observational conditions. In summary, HIP 89829 is a rapidly rotating young solar-type star with stable spot distribution, near-solid-body rotation, and a dominant poloidal global magnetic field.

ACKNOWLEDGEMENTS

The authors thank the referee for the constructive comments that helped improve this work.

We have made use of data from the European Space Agency's (ESA) mission *Gaia* (<https://www.cosmos.esa.int/gaia>), processed by the Gaia Data Processing and Analysis Consortium. Funding for the DPAC has been provided by national institutions, in particular the institutions participating in the Gaia Multilateral Agreement.

Observations collected in 2010 and 2011 used data obtained with HARPSpol (project ID 085.D-0296(B) and project ID 087.D-0771(A)) at the ESO 3.6-m telescope at La Silla.

This research was also aided by use of the SIMBAD database, operated at CDS, Strasbourg, France. A WWW interface to Simbad is available at: <http://simbad.u-strasbg.fr/Simbad>

DATA AVAILABILITY STATEMENT

The data underlying this paper will be shared on reasonable request to the corresponding author.

REFERENCES

Baliunas S. L. et al., 1995, *ApJ*, 438, 269
 Ballesteros F., 2012, *Europhys. Lett.*, 97, 34008
 Balona L. A., Abedigamba O. P., 2016, *MNRAS*, 461, 497
 Balthasar H., Vázquez M., Wöhl H., 1986, *A&A*, 155, 87
 Baraffe I., Homeier D., Allard F., Chabrier G., 2015, *A&A*, 577, A42
 Barnes J., Collier Cameron A., 2001, *MNRAS*, 326, 950
 Barnes J., Cameron A. C., James D., Donati J.-F., 2000, *MNRAS*, 314, 162
 Barnes J., Lister T., Hilditch R., Collier Cameron A., 2004, *MNRAS*, 348, 1321
 Bazot M. et al., 2018, *A&A*, 619, L9
 Berdyugina S. V., 2005, *Living Rev. Sol. Phys.*, 2, 1
 Bohm-Vitense E., 1981, *ARA&A*, 19, 295
 Brown S., Donati J.-F., Rees D., Semel M., 1991, *A&A*, 250, 463
 Brown A., et al., 2018, *A&A*, 616, A1

Brown E. et al., 2021, *MNRAS*, 501, 3981
 Burton D. M., 2013, PhD thesis, Univ. Southern Queensland
 Cameron A. C., 1992, in Byrne Patrick B., Mullan Dermott J., eds, Lecture Notes in Physics, Vol. 397, Surface Inhomogeneities on Late-Type Stars. Springer, Heidelberg, p. 33
 Cameron A. C., Donati J.-F., 2002, *MNRAS*, 329, L23
 Cang T.-Q. et al., 2020, *A&A*, 643, A39
 Carrington R., 1860, *MNRAS*, 20, 254
 Donati J.-F., Brown S., 1997, *A&A*, 326, 1135
 Donati J.-F., Cameron A. C., 1997, *MNRAS*, 291, 1
 Donati J.-F., Semel M., Carter B. D., Rees D., Cameron A. C., 1997, *MNRAS*, 291, 658
 Donati J.-F., Mengel M., Carter B., Marsden S., Collier Cameron A., Wichmann R., 2000, *MNRAS*, 316, 699
 Donati J.-F. et al., 2003, *MNRAS*, 345, 1145
 Donati J.-F., Forveille T., Cameron A. C., Barnes J. R., Delfosse X., Jardine M. M., Valenti J. A., 2006, *Science*, 311, 633
 Donati J.-F. et al., 2008, *MNRAS*, 385, 1179
 Fares R. et al., 2009, *MNRAS*, 398, 1383
 GAIA, 2016, GAIA Collaboration et al. (2016a): Summary description of Gaia DR1, Available at: <https://hdl.handle.net/2381/38739>
 Hale G. E., 1908, Contributions from the Mount Wilson Observatory, Vol. 1. Carnegie Institution of Washington, Washington, DC
 Hussain G., Prieto C. A., Saar S., Still M., 2006, *MNRAS*, 367, 1699
 Jeffers S., Donati J.-F., 2008, *MNRAS*, 390, 635
 Jeffers S., Barnes J., Collier Cameron A., 2002, *MNRAS*, 331, 666
 Jeffers S., Donati J.-F., Collier Cameron A., 2007, *MNRAS*, 375, 567
 Jeffers S., Donati J.-F., Alecian E., Marsden S., 2011, *MNRAS*, 411, 1301
 Jeffers S., Petit P., Marsden S., Morin J., Donati J.-F., Folsom C., 2014, *A&A*, 569, A79
 Jeffers S., Boro Saikia S., Barnes J., Petit P., Marsden S., Jardine M., Vidotto A., BCool Collaboration, 2017, *MNRAS*, 471, L96
 Kiraga M., 2012, *Acta Astron.*, 62, 67
 Lehtinen J., Jetsu L., Hackman T., Kajatkari P., Henry G., 2012, *A&A*, 542, A38
 Lehtinen J., Jetsu L., Hackman T., Kajatkari P., Henry G. W., 2016, *A&A*, 588, A38
 Marsden S., Waite I., Carter B., Donati J.-F., 2005, *MNRAS*, 359, 711
 Marsden S., Donati J., Semel M., Petit P., Carter B., 2006, *MNRAS*, 370, 468
 Marsden S. et al., 2011a, *MNRAS*, 413, 1922
 Marsden S. et al., 2011b, *MNRAS*, 413, 1939
 Maunder E. W., 1904, *MNRAS*, 64, 747
 Mengel M. et al., 2016, *MNRAS*, 459, 4325
 Messina S., Desidera S., Turatto M., Lanzafame A., Guinan E., 2010, *A&A*, 520, A15
 Petit P., Donati J.-F., Collier Cameron A., 2002, *MNRAS*, 334, 374
 Petit P. et al., 2008, *MNRAS*, 388, 80
 Petit P. et al., 2021, *A&A*, 648, A55
 PHASE C., 2003, *The Messenger*, 114, 20
 Rupprecht G. et al., 2004, in Moorwood Alan F. M., Masanori Iye, eds, Proc. SPIE Conf. Ser. Vol. 5492, Ground-based Instrumentation for Astronomy. SPIE, Bellingham, p. 148
 Schwabe M., 1843, *Astron. Nachr.*, 20, 283
 Semel M., 1989, *A&A*, 225, 456
 Skilling J., Bryan R., 1984, *MNRAS*, 211, 111
 Torres C., Quast G., Da Silva L., de La Reza R., Melo C., Sterzik M., 2006, *A&A*, 460, 695
 Torres C. A., Quast G. R., Melo C. H., Sterzik M. F., 2008, in Reipurth B., ed., ASP Conf. Ser., Vol. 5, Handbook of Star Forming Regions, Volume II: The Southern Sky. Astron. Soc. Pac., San Francisco, p. 757
 Valenti J. A., Fischer D. A., 2005, *ApJS*, 159, 141
 Vogt S. S., Penrod G. D., 1983, *PASP*, 95, 565
 Waite I., Marsden S., Carter B., Alecian E., Brown C., Burton D., Hart R., 2011, *Publ. Astron. Soc. Aust.*, 28, 323
 Waite I., Marsden S., Carter B., Petit P., Donati J.-F., Jeffers S., Boro Saikia S., 2015, *MNRAS*, 449, 8
 Willamo T. et al., 2019, *A&A*, 622, A170
 Wilson O., 1976, *ApJ*, 205, 823
 Wilson O., Woolley R., 1970, *MNRAS*, 148, 463

APPENDIX A: MAXIMUM ENTROPY FITS

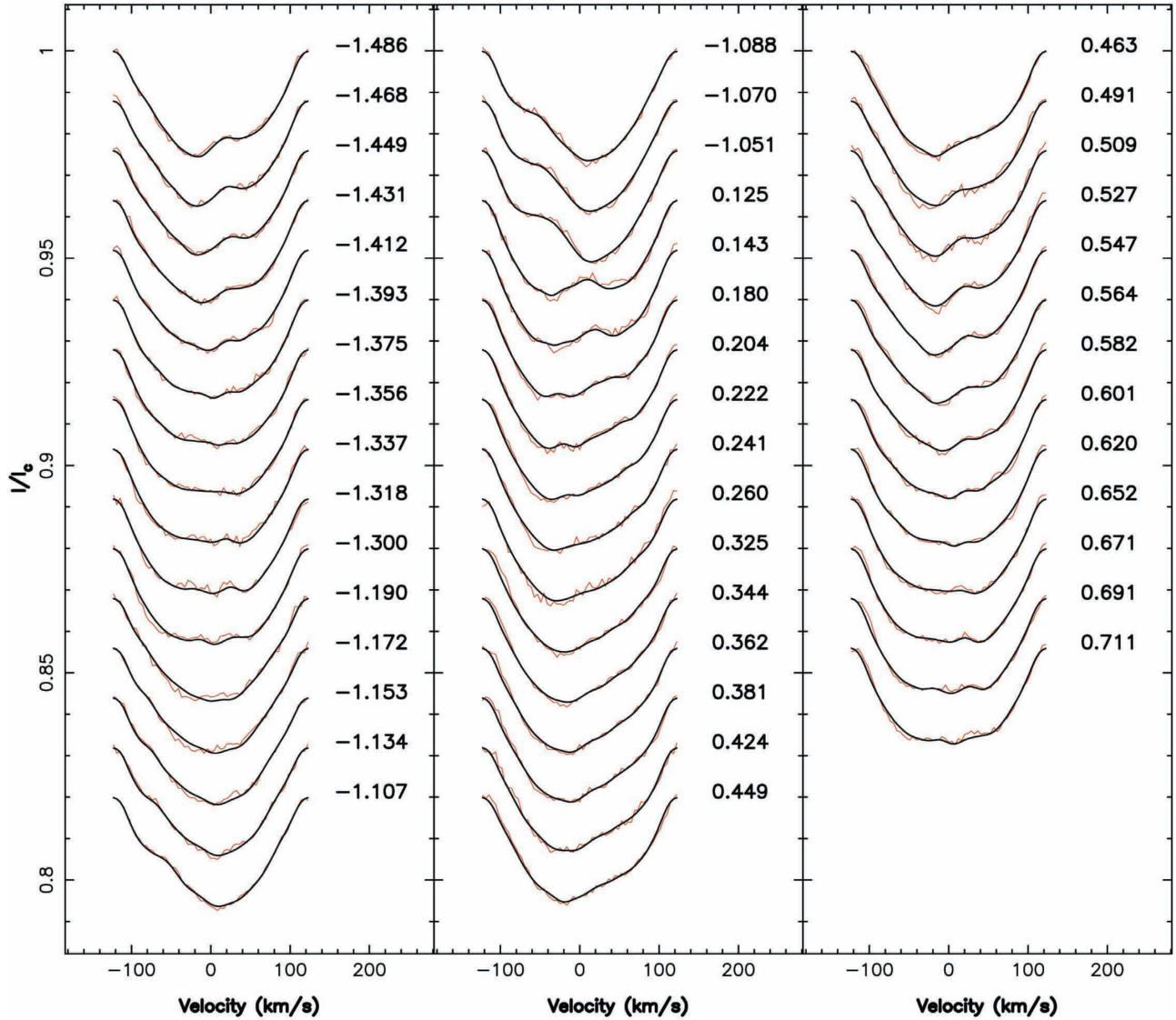


Figure A1. Maximum entropy fits for the Stokes I LSD profiles of HIP 89829 for epoch 2010.494. The red lines represent the observed LSD profiles, while the black lines represent the fits to the profiles produced by the imaging code. Each profile is shifted for graphical purposes. The rotational phases at which the observations took place are indicated to the right-hand side of each profile.

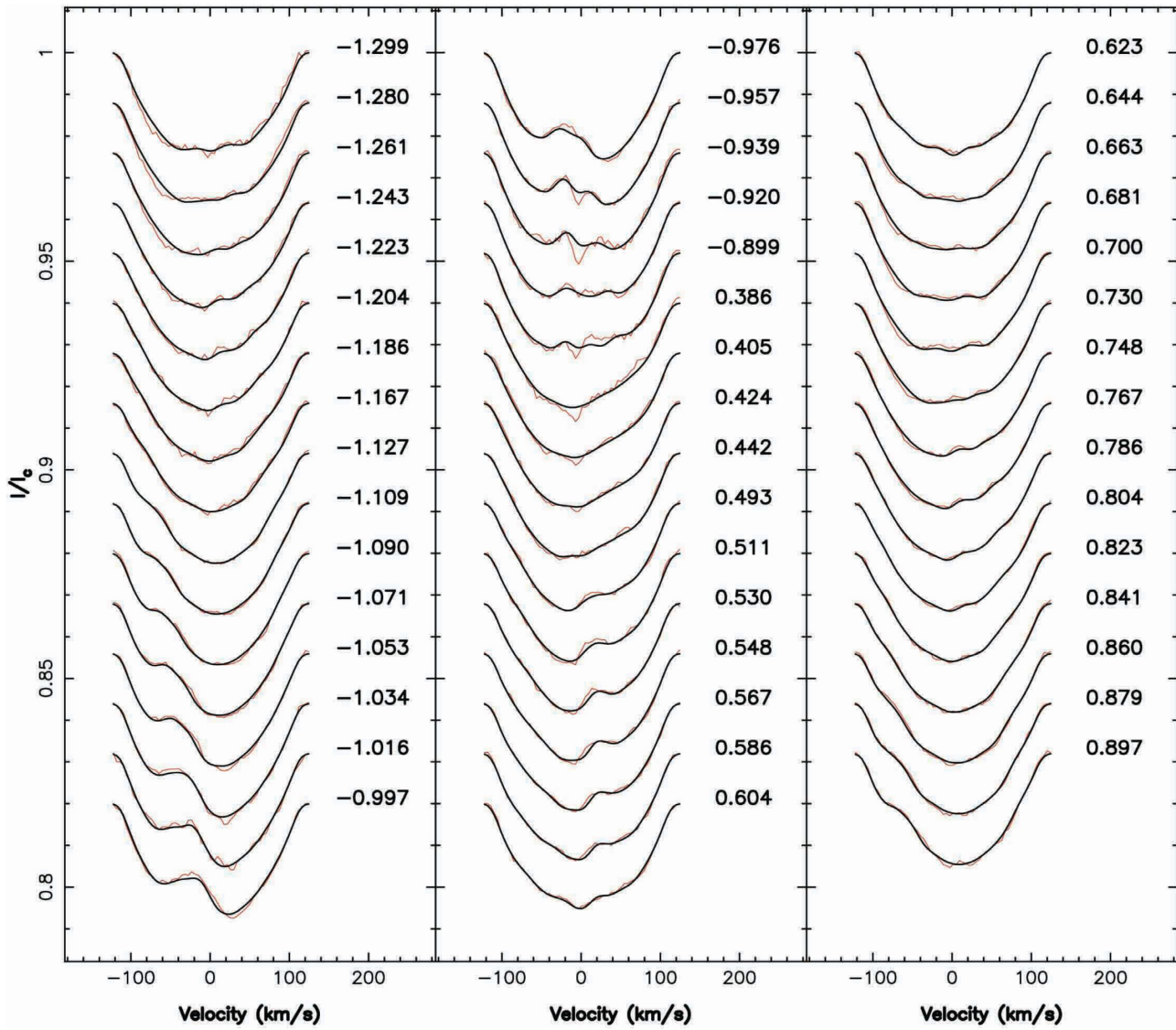


Figure A2. Maximum entropy fits for the Stokes I LSD profiles of HIP 89829 for epoch 2010.556. The layout is the same as Fig. A1.

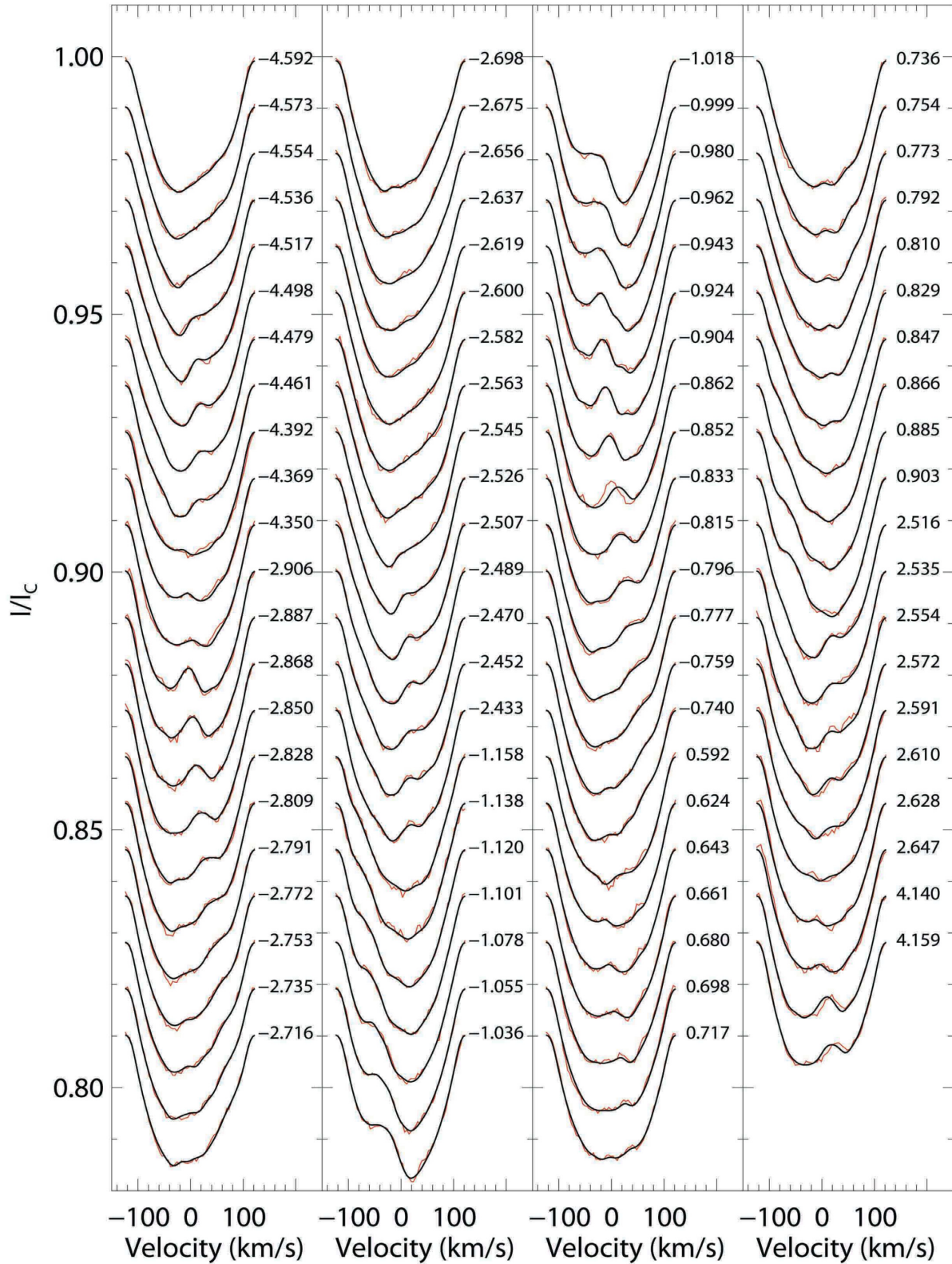


Figure A3. Maximum entropy fits for the Stokes I LSD profiles of HIP 89829 for epoch 2010.597. The layout is the same as Fig. A1.

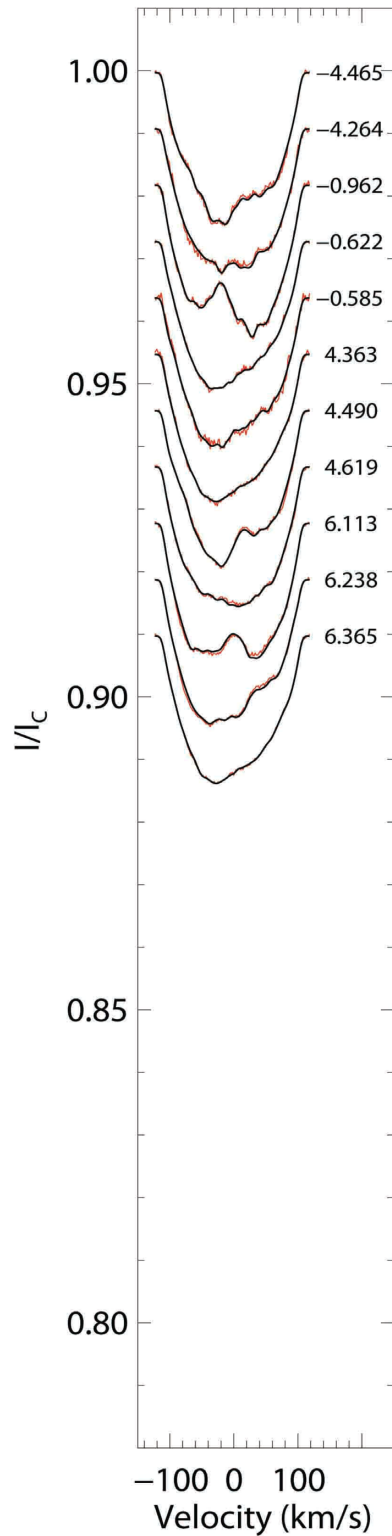


Figure A4. Maximum entropy fits for the Stokes I /LSD profiles of HIP 89829 for epoch 2010.613. The layout is the same as Fig. A1.

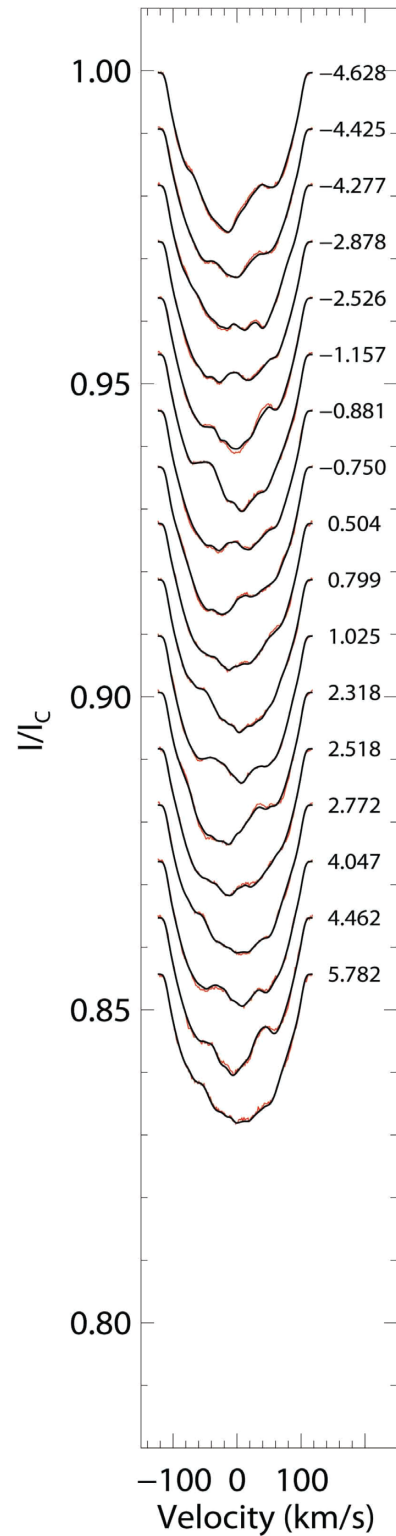


Figure A5. Maximum entropy fits for the Stokes I /LSD profiles of HIP 89829 for epoch 2011.378. The layout is the same as Fig. A1.

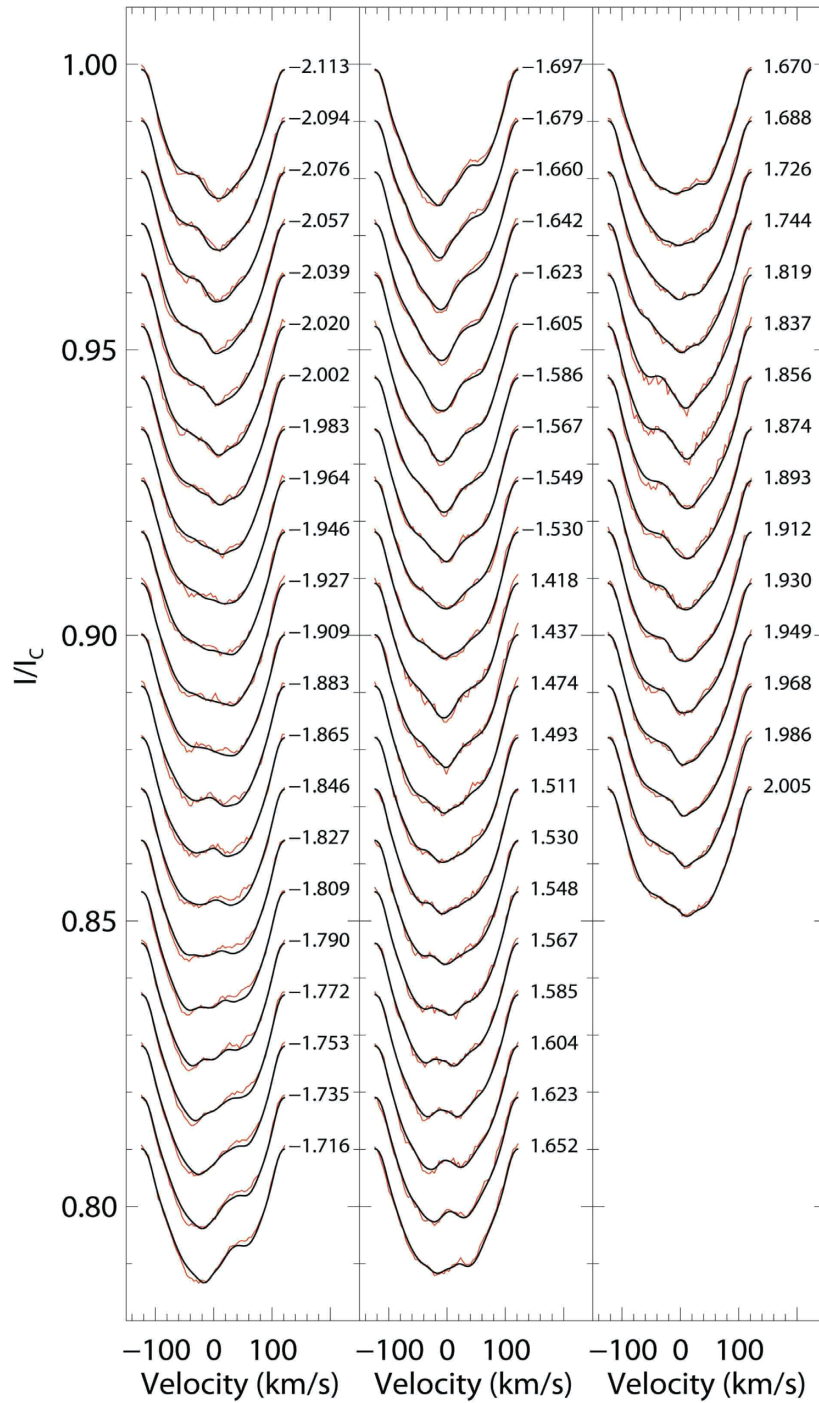


Figure A6. Maximum entropy fits for the Stokes I LSD profiles of HIP 89829 for epoch 2011.484. The layout is the same as Fig. A1.

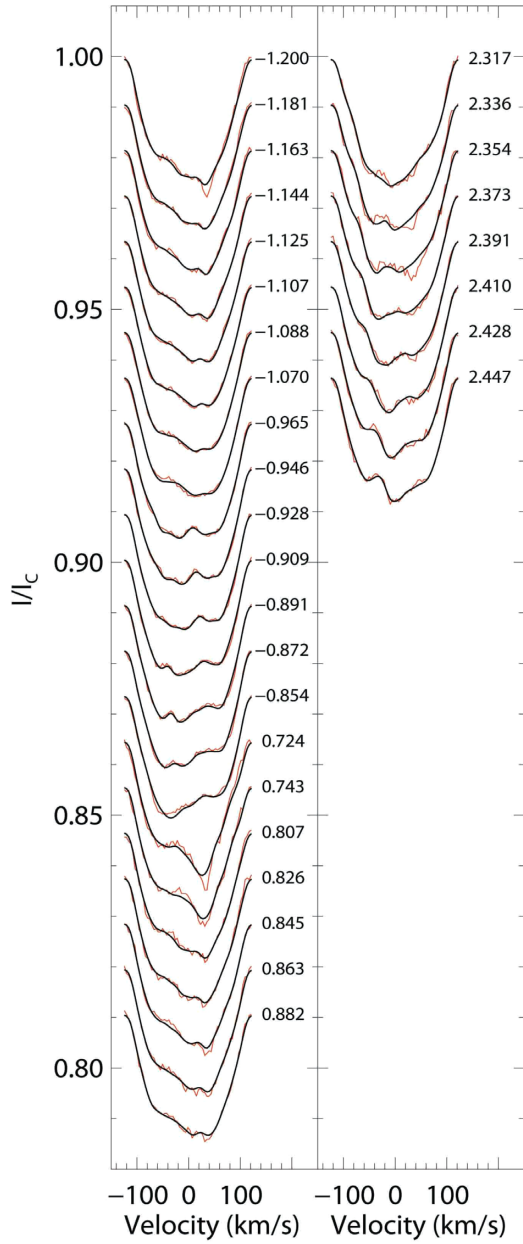


Figure A7. Maximum entropy fits for the Stokes I /LSD profiles of HIP 89829 for epoch 2012.272. The layout is the same as Fig. A1.

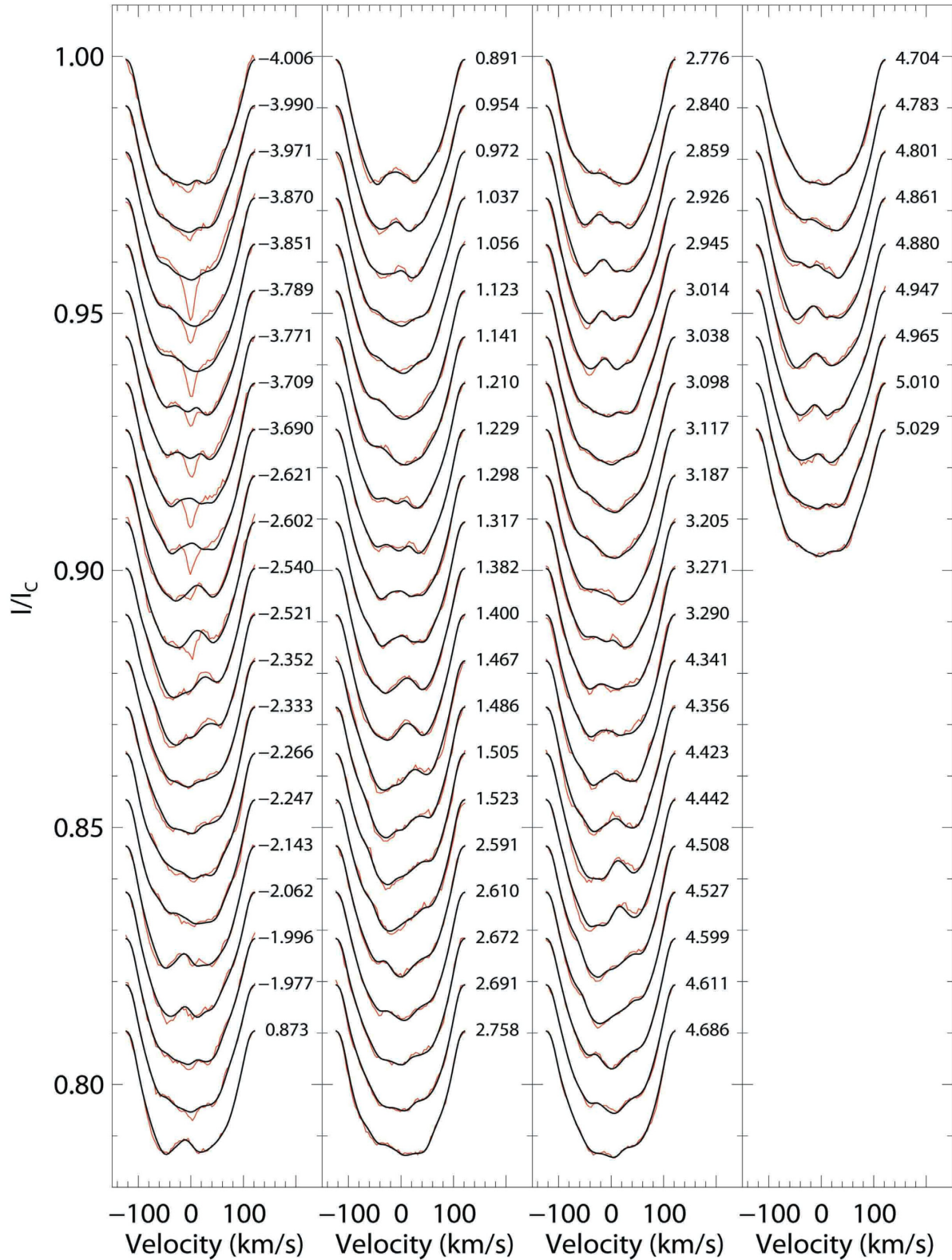


Figure A8. Maximum entropy fits for the Stokes I LSD profiles of HIP 89829 for epoch 2015.511. The layout is the same as Fig. A1.

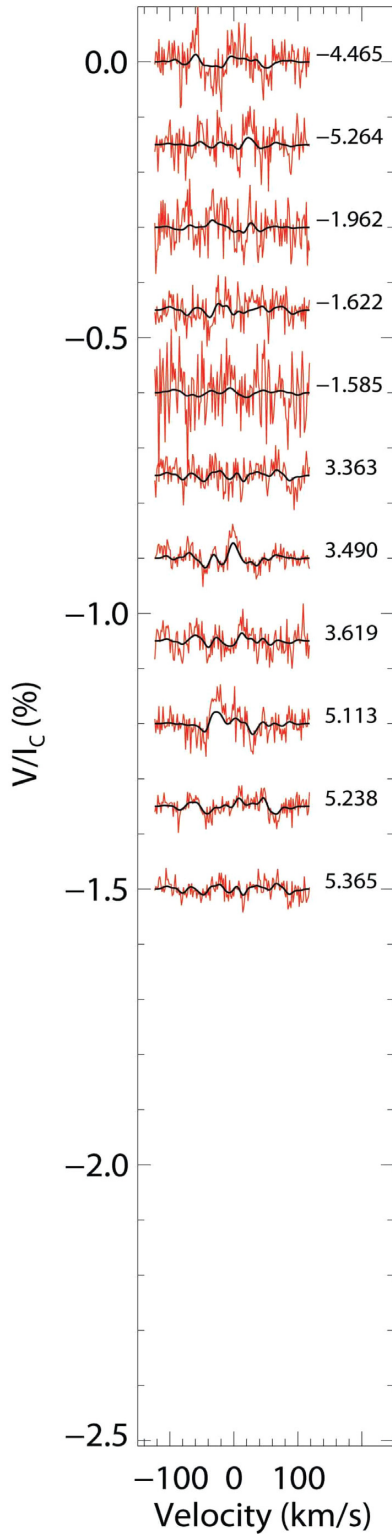


Figure A9. Maximum entropy fits for the Stokes V LSD profiles of HIP 89829 from the HARPSpol data set for epoch 2010.613. The red lines represent the observed LSD profiles, while the bolder black lines represent the fits to the profiles produced by the imaging code. Each profile is shifted down for graphical purposes. The rotational phases at which the observations took place are indicated to the right of each profile.

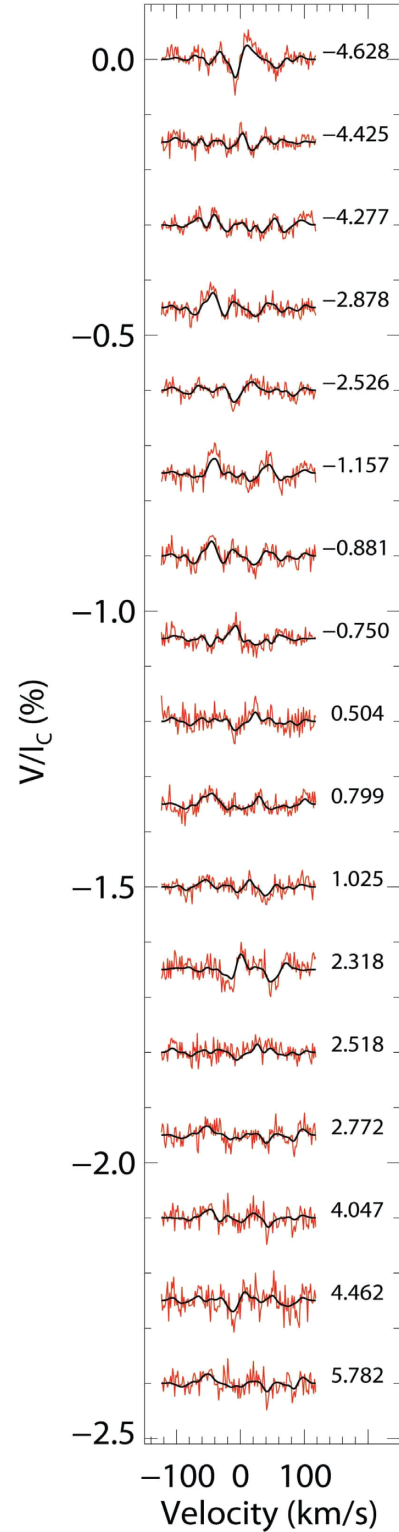


Figure A10. Maximum entropy fits for the Stokes V LSD profiles of HIP 89829 from the HARPSpol data set for epoch 2011.378. The layout is the same as Fig. A9.

This paper has been typeset from a $\text{\TeX}/\text{\LaTeX}$ file prepared by the author.